

Nano-cavity integrated van der Waals heterostructure light-emitting tunneling diode

Chang-Hua Liu¹, Genevieve Clark², Taylor Fryett³, Sanfeng Wu¹, Jiajiu Zheng³, Fariba Hatami⁴, Xiaodong Xu^{1,2*}, Arka Majumdar^{1,3*}

1. Department of Physics, University of Washington, Seattle, Washington 98195, USA.
2. Department of Materials Science and Engineering, University of Washington, Seattle, Washington 98195, USA.
3. Department of Electrical Engineering, University of Washington, Seattle, Washington 98195, USA.
4. Department of Physics, Humboldt University, D-12489 Berlin, Germany.

1. Device fabrication.

To prepare 2D materials, the hexagonal boron nitride (hBN) and graphene flakes were exfoliated onto SiO₂/Si substrates, and the WSe₂ flake was prepared by physical vapor transport growth.¹ For device applications, we selected the monolayer graphene, and WSe₂. For the tunneling barrier, we used 2 layers of hBN, because this thickness is optimal for achieving efficient tunneling and high brightness, as indicated in literature.² Their clearness and thickness are confirmed by optical contrast and atomic force microscopy. After collecting the required materials, we used the typical dry transfer technique³ to vertically stack these 2D flakes into van der Waals heterostructures (Gr/hBN/WSe₂/hBN/Gr). The stacked 2Ds were then transferred onto a Si/SiO₂ substrate, and cleaned with chloroform and isopropyl alcohol to remove the polymer residue coming from the transfer procedure. Electron beam lithography, metal deposition (5 nm/50 nm, Cr/Au), and lift-off processes were used to define electrodes, which are contacted with the top and bottom graphene layers separately. The electroluminescence was tested from this fabricated device before integrating with the photonic crystal cavity.

For photonic crystal cavity fabrication, we started with a 125nm thick Gallium phosphide (GaP) membrane with a sacrificial Aluminum gallium phosphide layer (AlGaP) on a GaP wafer. We defined an etch mask with 400 nm ZEP-520A that was patterned with a JOEL JBX-6300FS Electron Beam Lithography System. The pattern was transferred to the GaP thin film through Argon/Chlorine ICP dry etching. The resulting photonic crystal cavities were then cleaned in Dichloromethane and undercut with hydrofluoric acid so that the photonic crystal area is fully suspended. The final radius and period were nominally 53 nm and 200 nm, respectively.

To transfer the photonic crystal cavity onto the 2D heterostructures, we utilized the PDMS stamp to break the suspended photonic crystals from the GaP substrate (Figure S1a). The photonic crystals attached to the transfer stamp were then transferred onto a clean SiO₂/Si chip instead of directly onto 2D heterostructures (Figure S1b) to make sure that photonic crystals were not damaged by mechanical strain during the transfer procedure. Finally, we again used the dry transfer technique to transfer the selected cavity from the SiO₂ chip onto the light emitting WSe₂ area, and cleaned the entire device with chloroform and isopropyl alcohol.

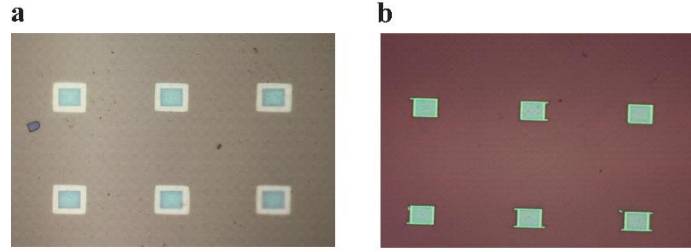


Figure S1 (a) Optical image of an array of suspended photonic crystals on the GaP substrate. (b) Optical image of photonic crystals transferred on the SiO₂/Si substrate.

2. Characterization of photonic crystal cavity with the cross-polarized reflectivity measurement.

To characterize the resonance wavelength of photonic cavity, we performed the cross-polarized reflectivity measurement.⁴ Specifically, the vertically polarized white light (from Fianium, whitelase micro supercontinuum laser) was focused on the cavity, which was placed at 45 degrees relative to the incoming polarization. The cavity polarizes the light to a basis that is 45 degrees to the incoming light. The horizontally polarized component of this light is then sent to the spectrometer. In order to further increase our signal to noise ratio we used a pinhole at the image plane of the confocal microscope to collect light coming only from the cavity.

Figure S2a shows the reflection spectrum, measured from a suspended photonic crystal cavity. Note that, the reflectivity spectrum shown here is from a similar cavity fabricated on the same chip, from where the hybrid LED is fabricated. Most of the cavities have similar quality factors, although different wavelengths. The spectrum at Figure S2a shows the resonance peak at 708 nm with the cavity quality factor ~1041. Some of these cavities are transferred to an oxide substrate to estimate the degradation of the cavity. Most cavities show red shift in the resonance and a large broadening. Figure S2b shows the reflectivity spectrum, measured from the cavity transferred on the SiO₂/Si substrate, which is used for fabricating hybrid LED. This cavity is then picked up from the oxide substrate and transferred onto the LED. The reflectivity spectrum of the cavity transferred on the 2d materials is inconclusive. Such degradation of cavity reflectivity is not unusual in photonic crystal platform. It is possible that multiple transfer processes and dirt introduce many scattering elements. These scattering elements change the incident polarization, and background reduction is not efficient for observing the cavity mode in cross-polarized reflectivity. From the EL (Figure 3, main text), we also observe a significant red-shift of the cavity mode and further degradation of the cavity quality factor. The exact reason behind this can be speculated to be a strain induced by the transfer process, or the change of surrounding refractive index after transferring the cavity onto 2Ds, as reported previously.⁵

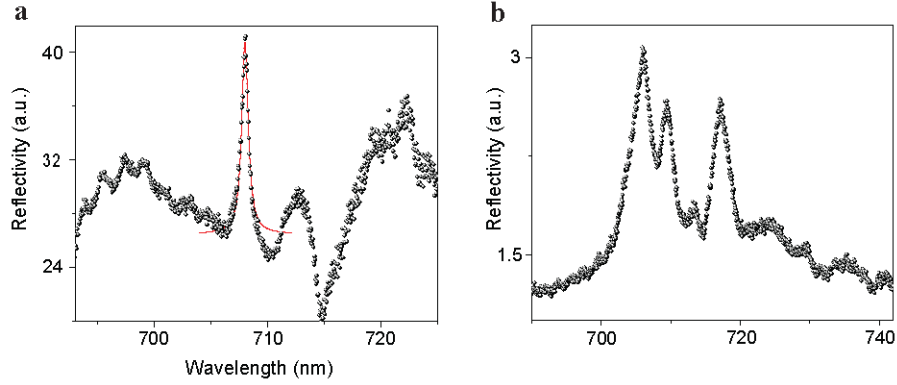


Figure S2 Cross-polarized reflection spectrum measured from (a) the photonic crystal cavity suspended on a GaP substrate, and (b) the photonic crystal cavity transferred onto the SiO₂/Si substrate. The black dots represent the measured reflection spectra and the red line represents the Lorentzian fitting of the cavity peak.

3. Characterization of the cavity-integrated light emitter with the photoluminescence measurement.

In addition to the reflectivity measurement, we also characterized the photoluminescence (PL) from the 2D heterostructures, integrated with the photonic crystal cavity. Figure S3 shows the measured x- and y-polarized PL spectra as the laser spot was focused on the cavity area. The direction of PL polarization is defined in Fig. 1d, inset in the main text, and the laser excitation wavelength is 633 nm with the excitation power at 30 μ W. The measured spectra clearly indicate that the cavity could enhance the spontaneous emission of WSe₂ \sim 759 nm and the cavity-enhanced emission is polarized in y direction, which are consistent with our EL measurements. However, we note the cavity-enhanced PL peak is not as evident in our EL measurements. This could be because we conducted the PL measurement in the last step, and the device has degraded after a series of EL characterizations. However, the reason for such degradation is not clear to us.

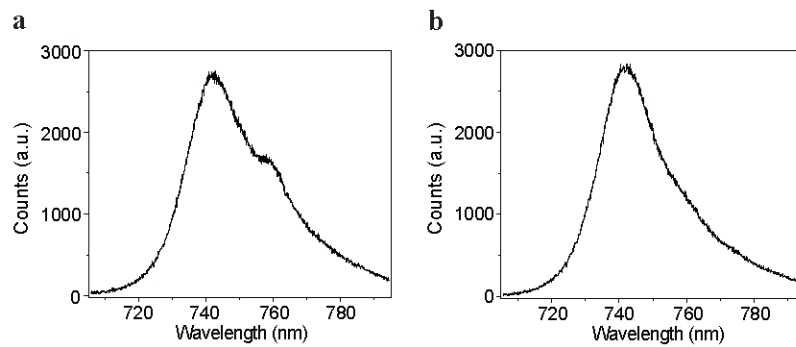


Figure S3 Characterization the cavity-integrated light emitter with photoluminescence measurements. (a) Resolving the linear y-polarized PL from the photonic cavity region. (b) Resolving the linear x-polarized PL from the photonic cavity region.

4. Evolution of bias-dependent EL measured from the cavity-integrated light emitter.

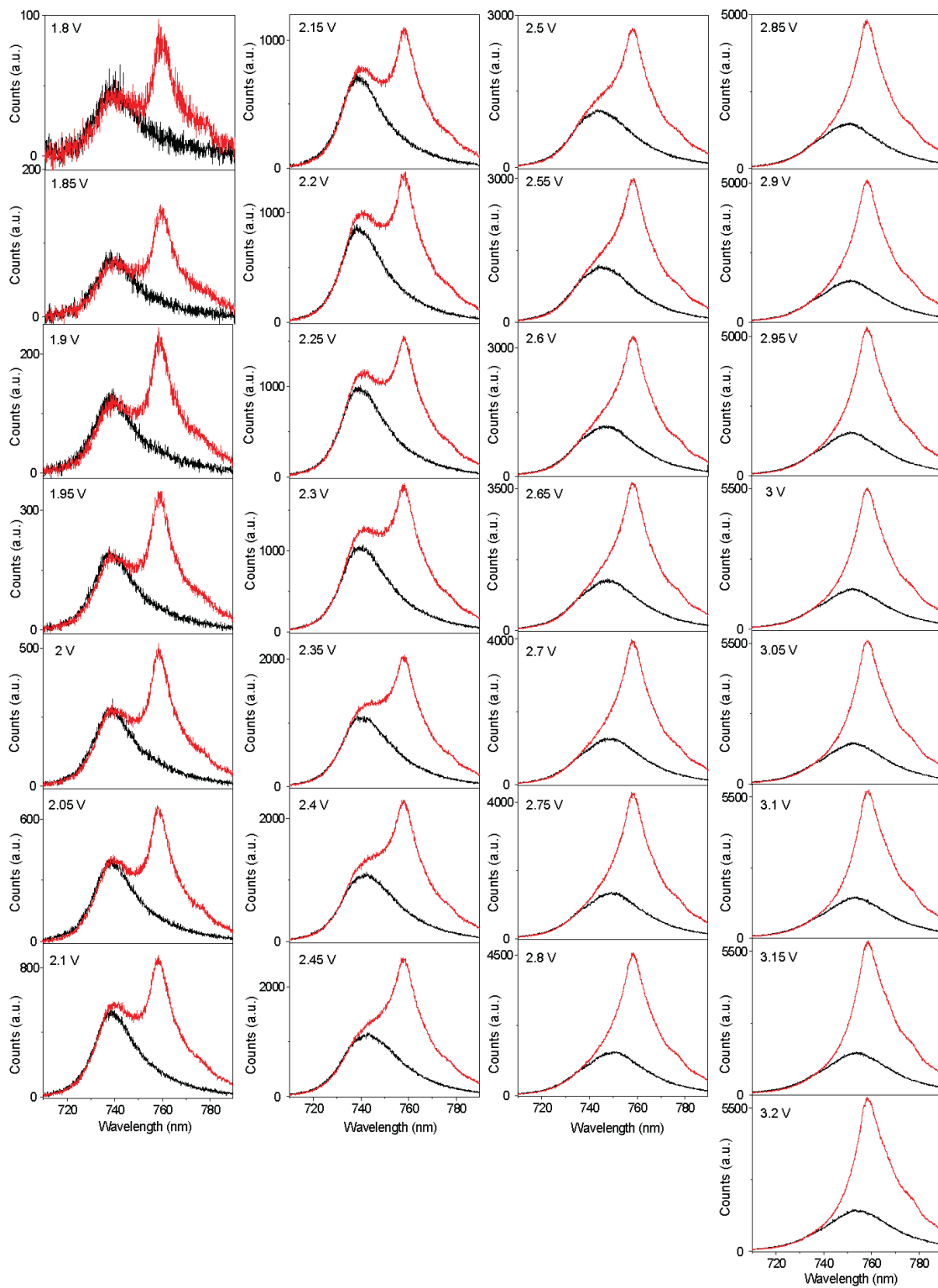
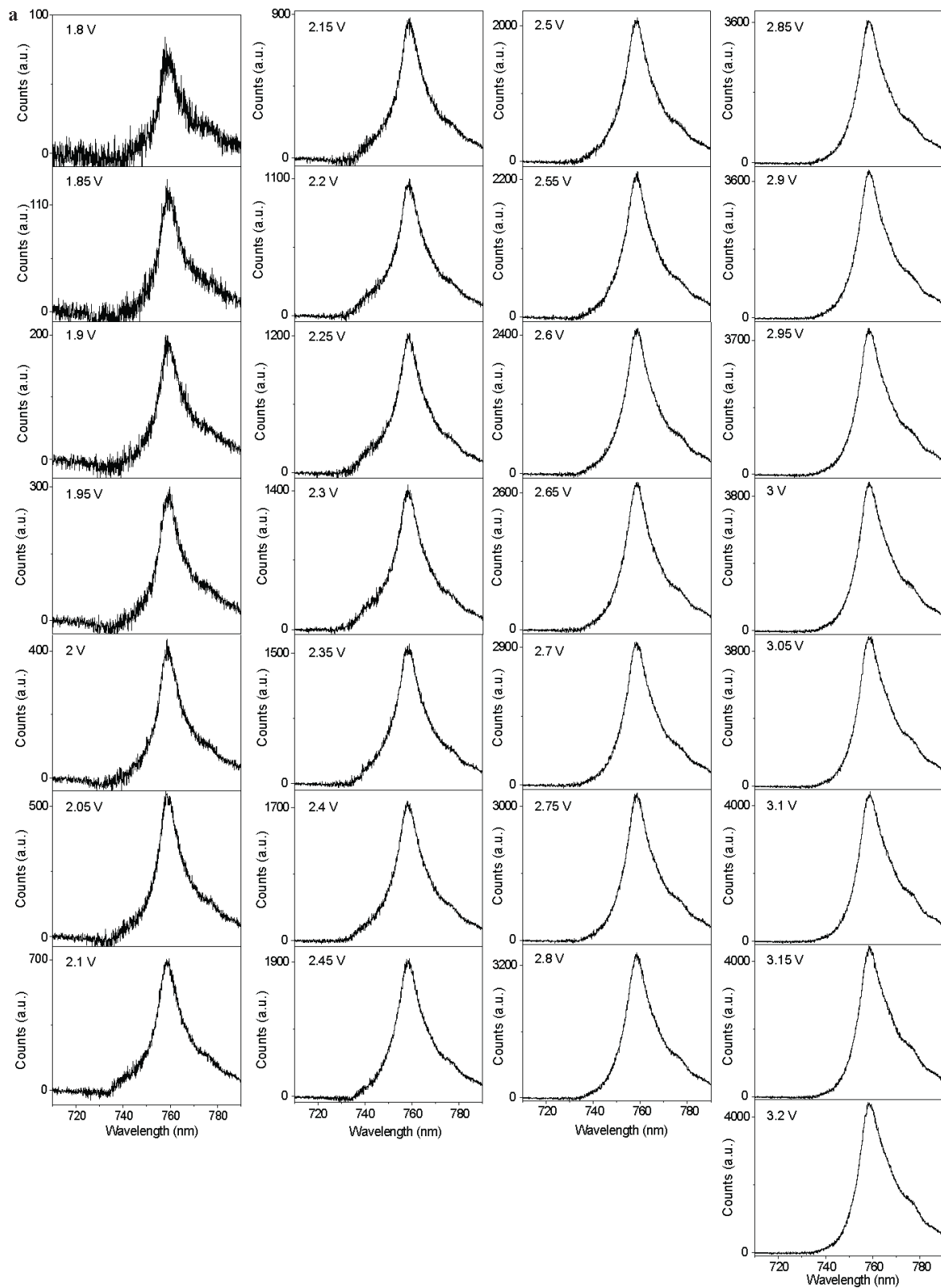


Figure S4 Resolving the x-polarized (black spectra) and y-polarized (red spectra) EL from the cavity-integrated light emitter as increasing the bias voltage.

5. Bias dependence of the lineshape and linewidth of cavity-enhanced EL.



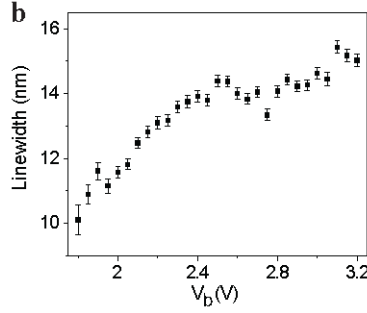


Figure S5 Lineshape and linewidth of the cavity-enhanced EL spectra. (a) Bias-dependent cavity enhanced EL by subtracting the cross-polarized EL from each other (y-polarized minus x-polarized EL shown in figure S4). (b) The full-width at half-maximum (FWHM) of cavity-enhanced EL, extracted from figure S5a, as a function of bias voltage.

6. Simulation of cavity degradation.

Initial cavity measurements were done immediately following their fabrication in order to determine the quality of the cavities. The resonances ranged from 700 – 800 nm with quality factors ranging from 1,000 – 8,000. The cavities were then broken off and transferred to a 300 nm thermal oxide substrate using the same dry transfer method as used for the 2D material transfer. Upon transfer the devices are re-characterized to establish how severely the cavities were degraded. FDTD simulations showed all cavity resonances having decreased quality factors and increased resonant wavelengths. The pristine cavity was simulated to have a fundamental mode with a quality (Q) factor of nearly 30,000 with the higher order modes being in the 1,000s. Once transferred the cavities were shown to have quality factors that were at best, nearly 1,000, but were nominally in the 100s. Given the cavity quality factor (~ 100) and the mode volume of $\sim 0.7 \left(\frac{\lambda}{n}\right)^3$, we expect the enhancement can reach 10. The cavities we measured were in good agreement with this result, thus we believe the oxide layer to be the dominant means by which the cavities were degraded.

7. Estimation of RC time constant and speed limit.

For our light emitting heterostructures, we estimate C_g is ~ 0.26 pF, given BN (2 layers, $\epsilon_{BN} = 4.5$)/WSe₂ (monolayer, $\epsilon_{WSe_2} = 4.5$)/BN (2 layers) vertically stacked in series and the overlapped area is $\sim 25 \mu m^2$. For series resistance, we note it is difficult to accurately extract the graphene/metal contact resistances simply based on this two terminal device. However, we could estimate the total series contact resistance will not be more than 100 kOhm. This value is calculated as the device is biased at 3.2 V (Fig. 1d, main text), and under such high bias, the tunneling junction becomes highly conducting and contact resistances become dominant.

Given $R = 100$ kOhms and $C = 0.26$ pF, we could calculate the operation speed is: $\frac{1}{2\pi \times 2.2RC \times 2} = 1.39$ MHz, which is close to our measurement result. The factor of 2π comes from the conversion from angular frequency to frequency. Furthermore, we use a factor of $2.2RC$ as we define the rise (decay) time to be the time interval between 10% - 90% (90% - 10%). The final factor of 2 is added as one cycle contains both a rise and a decay.

8. Estimation of external quantum efficiency.

To estimate the quantum efficiency of our device, we followed the calibration procedure as reported in literature.^{6,7} Briefly, the number of injected electrons and holes at different bias voltages can be calculated based on figure 1d. But to estimate the number of photons emitted from our device, we need to calibrate different loss terms, including the collection and transmission loss of objective lens, and the loss caused by confocal pinhole, gratings, and reflection components in our measurement systems. From these, we estimate the quantum efficiency of device can reach 0.2% (Figure S6). We note that the efficiency drops as increasing the bias voltage, and this might suggest high bias voltage (V_b) cause direct tunneling of carriers from graphene to graphene contact or high current density could lead to increased non-radiative recombination from the defect sites in CVD-grown WSe₂.⁸ Therefore, we expect the efficiency of device can be further enhanced by improving the quality of light emitting WSe₂ layer. Also, in terms of device structure, it is important to reduce the region, where two graphene contacts are overlapped without the WSe₂ sandwiched in between, to avoid direct tunneling between two graphene contacts.

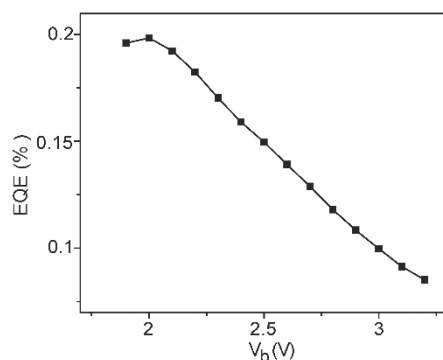


Figure S6 Bias-dependent external quantum efficiency of van der Waals light-emitting tunneling diode.

References:

1. Clark, G.; Wu, S.; Rivera, P.; Finney, J.; Nguyen, P.; Cobden, D. H.; Xu, X. *APL Mater.* **2014**, 2, 101101.
2. Withers, F.; Del Pozo-Zamudio, O.; Schwarz, S.; Dufferwiel, S.; Walker, P. M.; Godde, T.; Rooney, A. P.; Gholinia, A.; Woods, C. R.; Blake, P.; Haigh, S. J.; Watanabe, K.; Taniguchi, T.; Aleiner, I. L.; Geim, A. K.; Fal'ko, V. I.; Tartakovskii, A. I.; Novoselov, K. S. *Nano Lett.* **2015**, 15, 8223-8228.
3. Castellanos-Gomez, A.; Buscema, M.; Molenaar, R.; Singh, V.; Janssen, L.; van der Zant, H. S. J.; Steele, G. A. *2D Mater.* **2014**, 1, 011002.
4. Rivoire, K.; Faraon, A.; Vuckovic, J. *Appl. Phys. Lett.* **2008**, 93, 063103.
5. Gao, Y. D.; Shiue, R. J.; Gan, X. T.; Li, L. Z.; Peng, C.; Meric, I.; Wang, L.; Szep, A.; Walker, D.; Hone, J.; Englund, D. *Nano Lett.* **2015**, 15, 2001-2005.
6. Ross, J. S.; Klement, P.; Jones, A. M.; Ghimire, N. J.; Yan, J.; Mandrus, D. G.; Taniguchi, T.; Watanabe, K.; Kitamura, K.; Yao, W.; Cobden, D. H.; Xu, X. *Nature Nanotech.* **2014**, 9, 268-272.
7. Withers, F.; Del Pozo-Zamudio, O.; Mishchenko, A.; Rooney, A. P.; Gholinia, A.; Watanabe, K.; Taniguchi, T.; Haigh, S. J.; Geim, A. K.; Tartakovskii, A. I.; Novoselov, K. S. *Nature Mater.* **2015**, 14, 301-306.
8. Piprek, J. *Phys. Status Solidi A* **2010**, 207, 2217.